



High-temperature deformation followed *in situ* by X-ray microtomography: a methodology to track features under large strain

Pierre Lhuissier,^{a*} Therese Bormann,^a Guillaume Pelloux,^a Xavier Bataillon,^a Franck Pelloux,^a Charles Josserond,^a Pauline Gravier,^a Jean-Jacques Blandin,^a Elodie Boller^b and Luc Salvo^a

Received 28 August 2020

Accepted 31 January 2021

Edited by A. Stevenson, Australian Synchrotron, Australia

Keywords: *in situ* microtomography; high-temperature deformation; large strain; digital volume correlation.

^aUniversité Grenoble Alpes, CNRS, Grenoble INP, SIMAP, F-38000 Grenoble, France, and

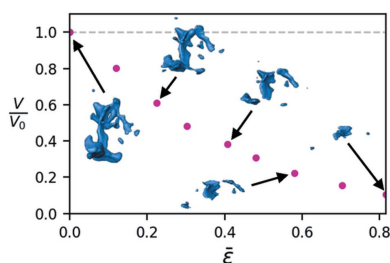
^bID19 Beamline, ESRF, 6 rue Jules Horowitz, BP 220, 38043 Grenoble Cedex 9, France.

*Correspondence e-mail: pierre.lhuissier@simap.grenoble-inp.fr

Metallic materials processing such as rolling, extrusion or forging often involves high-temperature deformation. Usually under such conditions the samples are characterized *post mortem*, under pseudo *in situ* conditions with interrupted tests, or *in situ* with a limited strain rate. A full *in situ* 3D characterization, directly during high-temperature deformation with a prescribed strain-rate scheme, requires a dedicated sample environment and a dedicated image-analysis workflow. A specific sample environment has been developed to enable highly controlled (temperature and strain rate) high-temperature deformation mechanical testing to be conducted while performing *in situ* tomography on a synchrotron beamline. A dedicated digital volume correlation algorithm is used to estimate the strain field and track pores while the material endures large deformations. The algorithm is particularly suitable for materials with few internal features when the deformation steps between two images are large. An example of an application is provided: a high-temperature compression test on a porous aluminium alloy with individual pore tracking with a specific strain-rate scheme representative of rolling conditions.

1. Introduction

Processing of metallic materials often requires high-temperature deformation (forging, rolling *etc.*). Under such high-temperature conditions, the mechanical behaviour of the materials can be highly sensitive to the applied strain rate (visco-plastic regime). Some deformation mechanisms are thermally activated and thus present a time dependency. The strain rate cannot be varied arbitrarily without potentially changing the predominant deformation mechanisms (dislocation glide, dislocation creep, diffusion, grain-boundary sliding *etc.*). During tests at constant strain rate, any interruption of the straining in order to perform an X-ray tomography scan is clearly detrimental, since it could induce a significant bias in the identification of the observed mechanisms. Thus, it is mandatory to be able to image the sample during straining without any change in either the strain rate or temperature. This often comes with large strain increments between 3D images due to the constraints of data flow and memory size of the camera. Similarly, when the strain-rate scheme is more complex, the tomography scans are preferentially performed during low-strain-rate segments and this also results in large strain increments. The strain-rate constraint also implies a trade-off on the acquisition time: a long exposure time and a large number of projections reduce



noise but increase potential blurring due to sample drift, deformation and the evolution of internal features. While some regularization can be applied to correct sample drift and sample straining (Ruhlandt *et al.*, 2017; Jailin & Roux, 2018; De Schryver *et al.*, 2018), internal feature evolution, the characterization of which is generally the purpose of the test, is hard to predict. As a consequence, one might need to reduce significantly the acquisition time, and thus the image quality, during a high-temperature deformation test.

The time required for a tomographic acquisition has decreased drastically during the last 20 years (Maire & Withers, 2014). While maximum acquisition rates were about 0.03 Hz in the early 2000s (Salvo *et al.*, 2003), 6 Hz could be achieved ten years later (Lhuissier *et al.*, 2012) and the current record is 200 Hz (García-Moreno *et al.*, 2019). The investigation of time-dependant mechanisms has thus become widely accessible to 3D imaging, with resolution at the microscale or even submicroscale (Villanova *et al.*, 2017).

Numerous sample environments have been developed in order to combine tomography imaging constraints and controlled sample thermomechanical loading. The simplest configurations relied only on thermal control of the sample, for example for the investigation of solidification. Furnaces have thus been developed based on resistors (Bellet *et al.*, 2003; Limodin *et al.*, 2009), lamps (Koster *et al.*, 1994; Grupp *et al.*, 2009; Sarin *et al.*, 2006), electromagnetic coils (Kudrna Prašek *et al.*, 2018), lasers (Fife *et al.*, 2012) *etc.* Micro-presses were developed in parallel to load the samples mechanically (Buffière *et al.*, 1999). The designs used various configurations depending on the organization of actuators, sensors, sample and rotating stage in the case of a cylindrical load-bearing system (Buffière *et al.*, 1999; Hufenbach *et al.*, 2012; Zauner *et al.*, 2012; Singh *et al.*, 2014; Gueninchault *et al.*, 2016; Pelerin *et al.*, 2019). Some designs include the heating system directly (Oswald *et al.*, 2013; Haboub *et al.*, 2014). The load-bearing system is usually made of polycarbonate, quartz, boron nitride, aluminium or carbon, depending on the thermomechanical constraints, imaged sample, load, heating system and so on. There is thus a strong coupling between the device design, the heating system, and the load-bearing tube material and dimensions. The requirements for a small bearing tube (reduced source-to-sample or sample-to-detector distances, small inductive coil) drastically reduce the system bending stiffness, which becomes highly sensitive to parasite motion at high acquisition rates when any device (actuator, sensor) is placed on top.

Configurations with all the main elements on the rotating-stage side (Zauner *et al.*, 2012; Gueninchault *et al.*, 2016; Pelerin *et al.*, 2019) clearly allow the optimization of the source-to-sample or sample-to-detector distance. A design using a fixed frame and two rotating stages makes the integration of the furnace close to the configuration of a standard laboratory testing device (Shade *et al.*, 2015). It also allows more complex loading, combining tension/compression and torsion (see, for example, the Deben 20 kN Open Frame X-ray Tensile/Compression and Torsion Tester). Nevertheless, it presents several drawbacks: a highly expensive design which

requires strong interference with the tomographic device (synchronization of rotating stages with the camera), a large footprint which might constrain the source-to-sample distance in conical beam configurations, and strong constraints on the rotation velocity which limit the acquisition rate to a few tenths of a hertz.

The requirement for a versatile non-intrusive micropress compatible with controlled high-temperature testing implies the development of a new system. Complete versatility on the type and size of sample tested, on the choice of imaging device and on the choice of heating system induces the following set of requirements:

- (i) Easy adjustment of load-cell capacity from 20 N to 2 kN.
- (ii) A large stroke (10 mm) with a submicrometre incremental step for high-resolution imaging.
- (iii) Easy per-sample design of the clamping system and load-bearing system.
- (iv) Complete independence of the sample's close environment from the sensor actuator.
- (v) A well equilibrated device in order to allow an acquisition rate up to several hertz.

Once the *in situ* X-ray microtomography characterization of the thermomechanical test has been conducted, an in-depth analysis of the data is performed to extract the required information. Amongst the targeted measurements, displacement or strain fields are often sought. In fact, knowledge of the kinematic fields allows us to make a proper link between the observations and a numerical twin, and can open up access to the stress field.

Most of the time, *in situ* tests are carried out in order to investigate the morphological evolution of some features: pores, dendrites, cracks *etc.* The ability to track these features from one acquisition step to the next is generally driven by the displacement field plus some morphological metrics. Measurement of the displacement field on the acquired data is thus a standard procedure based on digital volume correlation (DVC). Nevertheless, the general principle of DVC algorithms is an estimate of the transformation of the material's internal patterning. It is thus highly sensitive to a lack of internal patterning, to high noise and to large transformations.

When no thermally activated mechanisms are involved, small strain increments and long scan times do not affect the physical mechanisms involved. Thus, low-noise images with small strain increments are acquired and can feed classical DVC algorithms. Nevertheless, when the involved mechanisms are time-dependant, as is the case at high temperature, the imaging constraints are much stronger. The strain increments between two consecutive images can become very large and the signal-to-noise ratio weak. A sufficiently close estimate of the displacement field is required to allow the DVC algorithms to converge.

Global image transformation is not successful with heterogeneous strain fields. Multi-scale approaches cannot benefit from fine microstructural patterning at the coarse grain level and thus also fail to converge. There is thus a lack of a simple and generic enough DVC algorithm compatible with reduced image quality due to a high acquisition rate, limited sample

internal patterning, large deformations, a heterogeneous strain field and potentially huge datasets.

In the present experiment, a loading device able to control displacement and strain rate with a high accuracy on millimetre specimens, in both tension and compression, has been developed. The system is designed to allow high-temperature deformation with a fine temperature control. The overall system is compatible with fast *in situ* microtomography, meaning that it is compatible with scanning times of less than a few seconds with micrometre resolution. A specific work flow for data analysis has also been developed in order to estimate the strain field and to ensure automatic tracking of features of interest such as particles or pores. A specific DVC procedure has been implemented in order to handle large deformations between two images and limited sample internal patterning. Features of interest are then automatically tracked and analyzed even when they are highly changing (such as pore nucleation, pore closure, pore coalescence). Classical image-analysis procedures can then be easily applied to estimate morphological evolutions.

2. Devices and methods

High-temperature deformation requires a combination of a loading device and a heating system. The present device has been designed in order to allow continuous rotation on the tomography rotating stage. It consists of a loading system (actuator and sensor) coupled with a specific sample holder, compatible with several heating devices. The loading device stands on the rotating stage and thus turns continuously during X-ray microtomography acquisitions, while the furnace is fixed.

2.1. Loading device

The loading device is composed of a moto-reductor, gears, an endless screw, a moving cross tie, a load sensor and specific sample holders.

Fig. 1 presents the overall system composed of the device in a high-temperature compression configuration. The main components are labelled. A room-temperature tensile test configuration integrated in laboratory equipment is also presented.

Motion is ensured thanks to Maxon DC moto-reductors. A DCX 22L GB KL 36 V motor was selected. Two GPX22 C reductors are available: ratio 150:1 and ratio 35:1. The motor is equipped with a 1024 step encoder. A gear is screwed on the moto-reductor axis. Depending on the desired experimental conditions, the gear has 38 or 55 teeth. It is connected to a 120-tooth gear sealed to the endless screw. The gears have 0.5 mm teeth and are made of varying steel qualities depending on the required maximum load. All gears come from the HPC company. The endless screw rotates around a vertical axis thanks to a pre-strained ball bearing BEAS 008032-2RS from SKF. The endless screw is connected to a specific nut and both have been machined on purpose. The nut is connected to the moving cross tie. This cross tie is guided thanks to two ball

Table 1

Main characteristics of the two versions of the loading device.

Maximum stroke (mm)	10	25
Maximum load (kN)	2	5
Minimum velocity ($\mu\text{m s}^{-1}$)	1.3×10^{-2}	2.6×10^{-2}
Maximum velocity ($\mu\text{m s}^{-1}$)	1.0×10^3	2.0×10^3
Overall height (mm)	86	110

sleeves from Economax. On the cross tie stands a load cell. Depending on the required maximum load, a 20 N, 50 N, 200 N, 500 N, 2 kN or 5 kN load cell can be used (series 8523 and 8524 from Burster).

The load signal is amplified and converted to a 4–20 mA signal using an APJ-OEM from TEM. The signal is then converted to a 2–10 V signal by a 500 Ω resistor and recorded by an analogue USB module (USB-1408FS from Measurement Computing). The complete chain is calibrated on a laboratory tension/compression mechanical device (DY24 from ADAMEL) with a suitable load cell (calibrated every year by a certified company). A thermocouple transmitter from TC directly converts the signal from a K or an S thermocouple to a 4–20 mA current. The analogue USB module records the 2–10 V tension at the edges of the 500 Ω resistor.

Whatever the testing configuration (room temperature or high temperature), the load cell is kept at room temperature by forced air cooling (visible in Fig. 2). This ensures no load drift. Control of the moto-reductor is ensured by an EPOS 2 motor controller. Specific connectors are wired in order to make all the signal pass through the slip ring of the ESRF ID19 beamline rotating stage. The system can thus rotate *ad nauseam*.

The user interface is an in-house GUI based on Qt and proprietary Linux libraries. It enables the display of data,

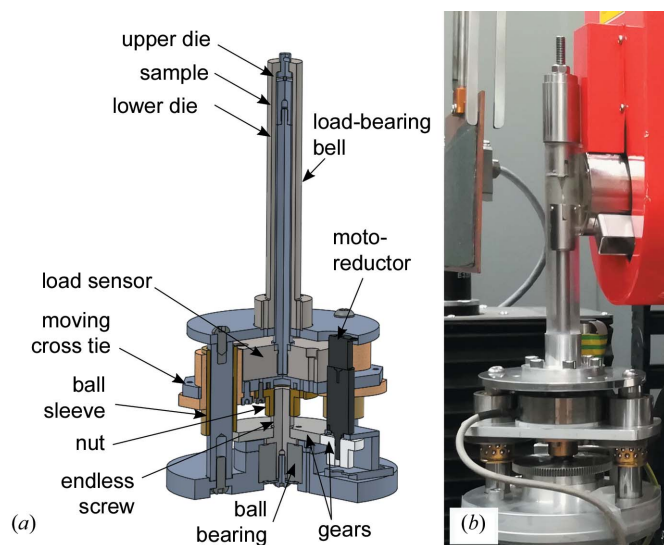


Figure 1 (a) A 3D rendering of the CAD of the system in the high-temperature compression configuration, with the main components labelled. (b) Integration in a laboratory apparatus in the room-temperature tensile configuration.

control of the motor (position, velocity, strain rate, limits *etc.*) and storage of data. The software is installed on a Raspberry Pi 2 computer.

Two compatible versions of the device exist. Table 1 summarizes the main characteristics of the two versions.

2.2. Heating systems

Depending on the testing temperature required, several heating devices can be used.

For tests up to 800°C, a resistive furnace is used. The furnace was developed by AET several years ago [see Limodin *et al.* (2009) for more details]. Its main characteristics are a maximum temperature of 800°C with a maximum heating rate of about 1°C s⁻¹. This furnace has two glassy carbon windows to allow the X-ray beam to go through. The furnace is placed on a ‘camera manipulator’ over the rotating stage and accurately aligned with the centre of rotation. A motor allows the furnace to move down to heat the sample. While in the down position, the sample is in the furnace, the X-ray beam goes through the glassy carbon windows and through the sample, and the sample can rotate freely around the vertical axis (tomographic rotation axis). A small horizontal translation of the sample (a few millimetres) inside the furnace is possible in order to move the sample out of the field of view and record reference images (also called ‘flat field’). Fig. 2 presents a view of the system integration on the ID19 beamline at the ESRF.

The furnace temperature and ramp rate are controlled in a dedicated *SPEC* session using a Eurotherm interface. Motors controlling the furnace motion are also integrated to the main *SPEC* session. The furnace temperature is recorded by *SPEC* and can also be used to trigger an experiment.

For temperatures higher than 800°C, inductive heating is used. It consists of a Hüttinger TIG5/300 system (rated power of 5 kW, adjustable coupling frequency from 30 to 300 kHz) with an in-house water-cooled copper coil. The coil axis is parallel to the rotation axis. A space between the coils allows a shadow-free path for the X-ray beam. Temperature is measured directly in the region of interest of the sample thanks to a fibre-optic bi-chromatic Impac IGAR 12-LO pyrometer (spectral lengths 1.52 µm/1.64 µm, adjustable optic from 200 to 350 mm corresponding to a measuring-spot diameter from 0.8 to 1.5 mm). The temperature is then manually monitored in order to avoid any instability. The power is manually adjusted with 0.1% accuracy.

The temperature of the sample is accurately calibrated using an original procedure relying on direct imaging. The system is too complex for a fine preliminary calibration. Indeed, the X-ray beam can induce some heating, and the sample holder, sample geometry, grips and sample position might change the temperature field. Thus an experimental calibration is performed every time the setup is installed on the beamline.

Samples made of predefined eutectic compositions allow the accurate measurement of some specific temperatures. For these eutectic compositions, by definition, the liquidus and



Figure 2
The high-temperature tensile test configuration on the ID19 beamline at ESRF. The sample environment rests on the rotating stage and is inserted in a fixed furnace. X-rays go through the furnace from right to left.

solidus become mixed up. The material changes from fully liquid to fully solid at a well known temperature. Melting or solidification is easily captured by visual observation of live radiographs during the calibration procedure. Melting temperature is not sensitive to a small change in the eutectic composition. Samples can be melted and solidified multiple times during the calibration procedure to allow fine adjustment of the furnace temperature with the sample melting temperature to about 1°C accuracy. It must be pointed out that the calibration is performed in the testing configuration, meaning that the eutectic can either have the size and shape of the sample and be placed in the mechanical device, or it can be a small eutectic part glued on the sample in the testing configuration.

The calibration thus provides a relationship between the furnace control temperature and the real sample temperature inside the testing device. Depending on the temperature range of the tests, different eutectics are used: Sn 9 wt% Zn (198°C), Al 54 wt% Ge (424°C), Al 33 wt% Cu (548°C), Al 6.1 wt% Ni (640°C), Cu 30 wt% Si (802°C), Ni 71.6 wt% Ti (942°C), Cu 9 wt% Zr (980°C), Ni 51.9 wt% Nb (1175°C) or Ni 23.2 wt% Nb (1282°C). The furnace temperature required

to reach the target sample temperature is then determined by linear interpolation. In this way, the temperature of the sample is accurately controlled. Note that accuracy is ensured for a constant-temperature test and does not account for inertia effects that would induce a deviation from the imposed thermal cycle.

2.3. Beamline integration

The system is integrated on the ID19 beamline at the ESRF. The loading system stands on a Leuven rotating stage. All signals go through a slip ring integrated inside the rotating stage. Data were reconstructed using ESRF *fasttomo3* pre-processing and *PyHST2* (Mirone *et al.*, 2014). Post-reconstruction ring removal was conducted using an in-house ESRF MATLAB code (Lyckegaard *et al.*, 2011). Data were cropped and converted to 8 bits using a fixed region of interest and range per sample. Post-processing was conducted using *ImageJ* (Schneider *et al.*, 2012) and in-house plugins (Boulos *et al.*, 2012).

2.4. Digital volume correlation

A dedicated DVC algorithm is implemented to deal with the specificities of such high-temperature tests, namely a large deformation between two images, a heterogeneous strain field and limited sample internal patterning. The correlation is performed in several steps. The principle of the algorithm is illustrated in Fig. 3.

First, features used for subsequent tracking are identified. Such features must be robust with respect to the cross-correlation algorithm. In other words, these features have to exhibit ‘large grey-level gradients’ in all directions, as well as small changes of shape from one stage to the other. The identification of these features is based on a 3D Harris corner-detection algorithm (Harris & Stephens, 1988) with a mask on the possible location of the points and an imposed minimum distance between selected points. The features are usually intermetallic second-phase particles which seldom evolve from one image to another. This initial set of points can be reduced depending on the region of interest. This set will be labelled ‘guiding points’. These guiding points are ordered based on the quality of the pattern. The larger the Harris

corner value (*i.e.* the absolute value of the smallest eigenvalue of the structure tensor), the higher the pattern quality for tracking purposes.

The guiding points are tracked from one image (labelled ‘initial image’) to the next one (labelled ‘final image’) in an iterative procedure. This relies on the cross correlation of a small parallelepipedal window (usually between 10 and 20 voxels in each dimension) centred on a guiding point in the initial image and the same parallelepipedal window translated (in three dimensions) in the final image. The cross correlation used here is a normalized cross correlation corrected from the average intensity in each image [as suggested by Doumalin (2000)]. The best cross-correlation coefficient is stored and used to define the matching position. If required, a rigid motion in rotation can also be applied. Nevertheless, these additional degrees of freedom are not usually used for computation cost efficiency. They seldom improve the accuracy of the results (at least for the specific materials and tests conducted in the present work).

The guiding points are sought in the final image within a ‘search window’ around a ‘guessed position’. The search window is usually anisotropic in order to match the maximal local motions which are larger in the tensile/compression direction. The size of the search window is several tens of voxels in each direction (usually about 50–80 in the tensile/compression direction and about 20–30 in the transverse direction). The search window of the first guiding point is enlarged by a factor of 5 to 8. This first point is sought in the final image around a guessed position which is equal to its position in the initial image. All other guiding points are sorted in a queue depending on their distance from any point of the queue (*i.e.* the point that is the closest to any point in the queue is the next one to be en-queued). Then the queue is processed. For each point, a guessed position in the final image is estimated. The guessed position is based on a weighted average of the positions of some guiding points already tracked. The average uses only points located within a given distance of the currently processed point in the initial image, whose already performed correlation factor is higher than a threshold. The average is weighted by a Gaussian of the distance. After processing the whole guiding-points queue, a first estimate of the position of the guiding points in the final image is available, and the quality of each tracking is assessed based on the correlation coefficient.

A second iteration of the tracking is then performed after some regularization, which consists in the identification of inconsistent positions. This is a direct implementation of the coherency estimation algorithm of Masullo & Theunissen (2016). The original algorithm was developed for particle image velocimetry (PIV) and is efficient for such heterogeneous displacement fields.

Guiding points within a given distance of the point of interest in the

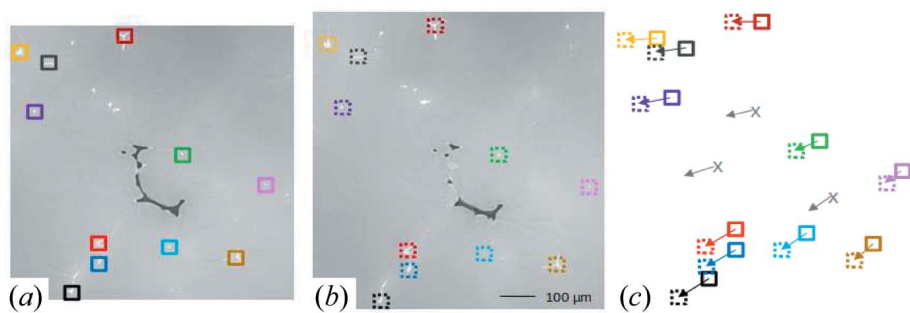


Figure 3
The principle of the DVC algorithm. Features are detected and tracked from (a) the reference state to (b) the deformed state in order to get an estimation of the displacement field at any point by interpolation: grey crosses in (c).

original image and with a correlation coefficient higher than a threshold are used to estimate the position of the point of interest in the final image. The position is estimated thanks to a quadratic fit of the displacement between the initial and final images. If the position found during the first correlation iteration is close to the fit, the point is considered valid (the correlated factor is kept unchanged). Otherwise it is considered to be badly correlated (the correlated factor is set to zero). All points are processed. The regularization algorithm is then run a second time to define the guessed position (thus badly correlated points are not accounted for to determine the guessed position). The cross correlation is then performed on all the guiding-points queue using these guessed positions and a reduced search window (usually the initial one divided by a factor of 2 to 4). The positions of the guiding points in the final image and the last correlation factor are stored.

The guiding points are then used to estimate the strain field and to track features of interest.

A mesh of eight noded bricks is defined over the region of interest. The displacement of each node is estimated based on a quadratic fit of the displacement of nearby guiding points with a sufficiently high correlation factor. A deformed mesh is thus defined. Initial and deformed meshes are then processed by a finite-element program, *Cast3M* (<http://www-cast3m.cea.fr/>), in order to compute local strain fields. Stress fields can also be computed with the same finite-element code using some of the experimental displacements as boundary conditions. However, this obviously requires one to provide as input a constitutive law. Note that with this implementation there is no optimization of the parameters of the constitutive law.

Virtual positions of features of interest in any image can be estimated using a similar quadratic fit on the guiding points. This enables features to be linked from one image to another, for example by using the label of the closest feature from the virtual position, either based on a features list or directly on a labelled image. Thus, it enables the evolution of features to be followed even when the objects are complex and/or elongated and split or merge.

The DVC and tracking procedure are implemented in C++ and CUDA in order to run on a general-purpose graphical processing unit (GPGPU) and benefit from the high degree of parallelism of the computation. The overall procedure lasts a couple of hours. Table 2 gives an example of computational time for one dataset. All outputs are written to VTK format in order to be visualized with *ParaView* (Ahrens *et al.*, 2005).

One must note that the scope of the DVC procedure is outside the elasticity regime. Most of the DVC approaches tackle sub-pixel displacements with complex shape functions in order to measure microstrain. The counterpart of such accuracy is the requirement for small strain increments between images, a small change in topology, a sufficiently patterned sample and limited noise in the images. Those algorithms fail to converge if a sufficiently close estimate is not provided. The proposed algorithm is designed to produce such an estimate. It does not target the microstrain accuracy. It is designed in order to provide an estimate of the strain field with an accuracy of a few percent for a sample with low internal

Table 2

Example of computational time for a given dataset.

Number of 3D images	8
Size of 3D images	1000 × 1000 × 670 voxels
Strain increment between images	5–20%
Number of guiding points	4600
Pattern window size	11 × 11 × 11 voxels
Search window size	41 × 41 × 101 voxels
Initial point search window size	161 × 161 × 401 voxels
Number of mesh cells	10 × 10 × 20
Number of tracked objects	~300
Processors	Intel Xeon E5-2605v3 @ 1.90 GHz
Number of processors	2
Number of cores per processor	6
GPU	Quadro K4200
Average total time	2 h 30 min

patterning, a strain between two images as large as several tens of percent, large topological changes of some features and strong strain heterogeneities.

3. Application

3.1. Materials and tests

A single example is presented here: the high-temperature compression of an as-cast 2050 aluminium alloy sample presenting large solidification pores. A specific strain-rate scheme was applied to mimic a rolling scheme: a succession of high-strain-rate segments and holding times. Cylindrical samples with a diameter of 2 mm and a height of 2 mm were compressed at 480°C with alternating relatively high-strain-rate steps (about 1 s⁻¹ over 200 µm die displacement, meaning roughly 10% strain steps) and 1 min holding time. The sample was placed in a boron nitride bell and compressed between two Inconel dies. A 34 keV X-ray beam illuminated the sample. Data were recorded with a PCO edge detector coupled to a 100 µm thick YAG scintillator with a ×5 optic. A total of 2000 radiographs of 1536 × 1440 pixels were recorded for each scan in 10 s between successive compression steps, while keeping the sample in the furnace.

3.2. Results

The proposed example was aimed at identifying a criterion for pore closure during high-temperature compression. The determination of the displacement field is mandatory to obtain the local stress field. The large deformation endured by the sample between two successive images requires a robust algorithm. The displacement field is also required to connect the pores from one time step to the next. The device and the tracking procedure both proved to be efficient. The inter-metallics chosen as guiding points are branched and relatively homogeneously distributed in the sample. This set of guiding points is thus robust and dense enough to estimate the displacement field in the whole sample. Fig. 4 presents an overview of the analysis performed on a sample: a 3D pore view, the strain field, and the relationship between the volume of a given pore and the cumulative local strain.

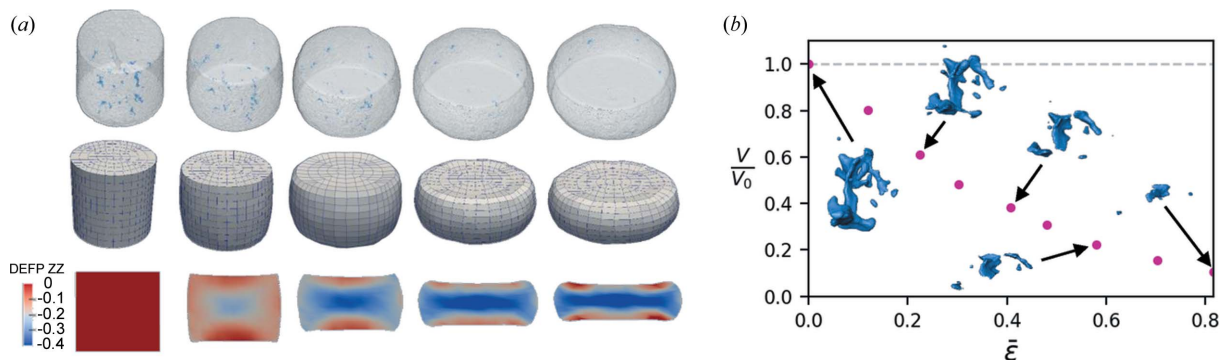


Figure 4 (a) (Top) 3D views of the porosity in the sample, (middle) mesh deformation measured by DVC and (bottom) the associated strain field (ϵ_{zz} component) in a vertical cross section for all the compression steps. (b) The evolution of the volume of a single pore as a function of the cumulative local strain.

The mesh obtained by DVC is consistent with the sample geometry changes. The strain field also appears to be consistent with the applied loading. The displacement field allowed the accurate prediction of the pore positions from one time step to the next. The tracking thus enabled the evolution of a pore's relative volume change to be plotted as a function of the local strain field as well as the integral of stress triaxiality. The validity of such a criterion for pore-closure prediction can thus be investigated using this approach.

4. Conclusions

A versatile tension/compression device has been developed. The device is compatible with the constraints of fast synchrotron X-ray microtomography and the fine thermal control required for high-temperature tests. A specific digital volume-correlation (DVC) algorithm has been set up and efficiently implemented in order to make it suitable to handle *in situ* synchrotron high-temperature tests that lead to reduced image quality due to the high acquisition rate, limited sample internal patterning, large deformations, heterogeneous strain field and potentially huge datasets. The device has been validated based on a wide variety of high-temperature deformation tests.

The DVC procedure has been applied to aluminium samples presenting a limited sample internal patterning with a large deformation between two successive steps. The obtained displacement field was reliable since it allowed the pores to be tracked during the process. The application of the displacement field as a boundary condition for finite-element simulations gave access to the local stress field. This information can easily be combined to follow, for a given porosity, morphological parameters such as pore volume and aspect ratio as a function of strain or stress components.

The versatility of the system allows the easy expansion of the current field of investigation. For example, it could be implemented with an X-ray laboratory source to perform room-temperature mechanical tests. The acquisition conditions can be optimized for each type of sample by selecting a suitable load-bearing bell. The DVC procedure has been successfully applied to a wide range of acquisitions: *in situ* nanotomography high-temperature tensile tests (Kumar *et al.*,

2019), *in situ* micro-CT firm densification (Burr, 2017) and *in situ* unfolding of corrugated struts produced by additive manufacturing (Suard *et al.*, 2020).

Funding information

The European Radiation Synchrotron Facility (ESRF) is acknowledged for the long-term project MA1876, 'Use of coherency and large field of view for fast *in situ* multi-resolution imaging', and for the MA3484 beamtimes. The Agence Nationale de la Recherche is acknowledged for a post-doctoral grant to Therese Bormann in the framework of the EDDAM project. C-TEC/Constellium is acknowledged for PhD funding for Pauline Gravier.

References

Ahrens, J., Geveci, B. & Law, C. (2005). *ParaView: An End-User Tool for Large Data Visualization. The Visualization Handbook*, Vol. 717. Munich: Elsevier.

Bellet, D., Gorges, B., Dallery, A., Bernard, P., Pereiro, E. & Baruchel, J. (2003). *J. Appl. Cryst.* **36**, 366–367.

Boulos, V., Fristot, V., Houzet, D., Salvo, L. & Lhuissier, P. (2012). *Proceedings of the 6th Annual Conference on Design and Architectures for Signal and Image Processing (DASIP)*, 23–25 October 2012, Karlsruhe, Germany, pp. 1–6. IEEE.

Buffière, J. Y., Maire, E., Cloetens, P., Lormand, G. & Fougères, R. (1999). *Acta Mater.* **47**, 1613–1625.

Burr, A. (2017). PhD thesis, Université Grenoble Alpes, France.

De Schryver, T., Dierick, M., Heyndrickx, M., Van Stappen, J., Boone, M. A., Van Hoorebeke, L. & Boone, M. N. (2018). *Sci. Rep.* **8**, 7655.

Doumalin, P. (2000). PhD thesis, Ecole Polytechnique X, Palaiseau, France.

Fife, J. L., Rappaz, M., Pistone, M., Celcer, T., Mikuljan, G. & Stampanoni, M. (2012). *J. Synchrotron Rad.* **19**, 352–358.

García-Moreno, F., Kamm, P. H., Neu, T. R., Bülk, F., Mokso, R., Schlepütz, C. M., Stampanoni, M. & Banhart, J. (2019). *Nat. Commun.* **10**, 3762.

Grupp, R., Henkel, F., Nöthe, M., Banhart, J., Kieback, B. & Haibel, A. (2009). *J. Synchrotron Rad.* **16**, 524–527.

Gueninchault, N., Proudhon, H. & Ludwig, W. (2016). *J. Synchrotron Rad.* **23**, 1474–1483.

Haboub, A., Bale, H. A., Nasiatka, J. R., Cox, B. N., Marshall, D. B., Ritchie, R. O. & MacDowell, A. A. (2014). *Rev. Sci. Instrum.* **85**, 083702.

Harris, C. & Stephens, M. (1988). *Proceedings of the Alvey Vision Conference 1988*, pp. 23.1–23.6. Manchester: Alvey Vision Club.

- Hufenbach, W., Böhm, R., Gude, M., Berthel, M., Hornig, A., Ručevskis, S. & Andrich, M. (2012). *Compos. Sci. Technol.* **72**, 1361–1367.
- Jailin, C. & Roux, S. (2018). *Materials*, **11**, 1395.
- Koster, A., Fleury, E., Vasseur, E. & Remy, L. (1994). *Automation in Fatigue and Fracture: Testing and Analysis*, edited by C. Amzallag, pp. 563–580. West Conshohocken, Pennsylvania, USA: ASTM International.
- Kudrna Prašek, M., Pistone, M., Baker, D. R., Sodini, N., Marinoni, N., Lanzafame, G. & Mancini, L. (2018). *J. Synchrotron Rad.* **25**, 1172–1181.
- Kumar, R., Villanova, J., Lhuissier, P. & Salvo, L. (2019). *Acta Mater.* **166**, 18–27.
- Lhuissier, P., Scheel, M., Di Michiel, M., Boller, E., Adrien, J., Maire, E., Salvo, L., Blandin, J.-J. & Suery, M. (2012). *Proceedings of the 1st International Conference on 3D Material Science*, 8–12 July 2012, Seven Springs, Pennsylvania, USA, pp. 203–208.
- Limodin, N., Salvo, L., Boller, E., Suéry, M., Felberbaum, M., Gailliègue, S. & Madi, K. (2009). *Acta Mater.* **57**, 2300–2310.
- Lykkegaard, A., Johnson, G. & Tafforeau, P. (2011). *Int. J. Tomogr. Stat.* **18**, 1–9.
- Maire, E. & Withers, P. J. (2014). *Int. Mater. Rev.* **59**, 1–43.
- Masullo, A. & Theunissen, R. (2016). *Exp. Fluids*, **57**, 33.
- Mirone, A., Brun, E., Gouillart, E., Tafforeau, P. & Kieffer, J. (2014). *Nucl. Instrum. Methods Phys. Res. B*, **324**, 41–48.
- Oswald, B. B., Schuren, J. C., Pagan, D. C. & Miller, M. P. (2013). *Rev. Sci. Instrum.* **84**, 033902.
- Pelerin, M., King, A., Laiarinandrasana, L. & Proudhon, H. (2019). *Integr. Mater. Manuf. Innov.* **8**, 378–387.
- Ruhlandt, A., Töpferwien, M., Krenkel, M., Mokso, R. & Salditt, T. (2017). *Sci. Rep.* **7**, 6487.
- Salvo, L., Cloetens, P., Maire, E., Zabler, S., Blandin, J., Buffière, J., Ludwig, W., Boller, E., Bellet, D. & Josserond, C. (2003). *Nucl. Instrum. Methods Phys. Res. B*, **200**, 273–286.
- Sarin, P., Yoon, W., Jurkschat, K., Zschack, P. & Kriven, W. M. (2006). *Rev. Sci. Instrum.* **77**, 093906.
- Schneider, C. A., Rasband, W. S. & Eliceiri, K. W. (2012). *Nat. Methods*, **9**, 671–675.
- Shade, P. A., Blank, B., Schuren, J. C., Turner, T. J., Kenesei, P., Goetze, K., Suter, R. M., Bernier, J. V., Li, S. F., Lind, J., Lienert, U. & Almer, J. (2015). *Rev. Sci. Instrum.* **86**, 093902.
- Singh, S. S., Williams, J. J., Hruby, P., Xiao, X., De Carlo, F. & Chawla, N. (2014). *Integrating Mater.* **3**, 109–122.
- Suard, M., Plancher, E., Martin, G., Dendievel, R. & Lhuissier, P. (2020). *Adv. Eng. Mater.* **22**, 2000315.
- Villanova, J., Daudin, R., Lhuissier, P., Jauffrès, D., Lou, S., Martin, C. L., Labouré, S., Tucoulou, R., Martínez-Criado, G. & Salvo, L. (2017). *Mater. Today*, **20**, 354–359.
- Zauner, M., Keunecke, D., Mokso, R., Stampanoni, M. & Niemz, P. (2012). *Holzforchung*, **66**, 973–979.